ARMA 16-239

# Micro-mechanical analysis of salt creep tests with a joint-enriched Finite Element model

Zhu, C.[1], Pouya, A.[2], Arson, C.[1], Ding, J.[3], Chester, F.M.[3], and Chester, J.S.[3]

[1]*School of Civil and Environmental Engineering, Georgia Institute of Technology, Atlanta, Georgia*

[2]*Laboratoire Navier (IFSTTAR, CNRS, ENPC), Paris-Est University, Champs sur Marne, France*

[3]*Department of Geology and Geophysics, Texas A&M University, College Station, Texas*



This paper was prepared for presentation at the 50th US Rock Mechanics / Geomechanics Symposium held in Houston, Texas, USA, 26-29 June 2016. This paper was selected for presentation at the symposium by an ARMA Technical Program Committee based on a technical and critical review of the paper by a minimum of two technical reviewers. The material, as presented, does not necessarily reflect any position of ARMA, its officers, or members. Electronic reproduction, distribution, or storage of any part of this paper for commercial purposes without the written consent of ARMA is prohibited. Permission to reproduce in print is restricted to an abstract of not more than 200 words; illustrations may not be copied. The abstract must contain conspicuous acknowledgement of where and by whom the paper was presented.

**ABSTRACT:** In this study, micro-mechanisms that govern the viscous and damage behavior of salt polycrystal during creep processes are investigated. A Finite Element model is designed with POROFIS, in which surface elements represent salt grains and joint elements represent inter-granular contacts. Microscopic observations of salt thin sections serve as a basis to design the mesh, which includes voids. We compare three strategies to predict microscopic damage in the salt polycrystal: (1) inter-granular damage represented by damage propagation in joint elements; (2) intra-granular damage represented by stiffness degradation in grain surface elements; (3) damage in both surface and joint elements. We simulate creep tests in conditions typical of Compressed Air Energy Storage. The three models capture polycrystal stiffness degradation and the initiation, propagation and coalescence of cracks that originate from geometric incompatibilities and local stress concentrations. The model with damageable joints presents a more ductile behavior and captures a smooth transition between steady state and tertiary state creep. This research is expected to improve the fundamental understanding of viscous damage mechanisms in salt rock for geostorage applications, and bring new insights on numerical modeling of multi-scale damage processes in crystalline materials.

## 1. INTRODUCTION

Because of its low gas permeability, high solubility in water, favorable creep properties and fast self-healing potential, salt rock is considered as an appropriate host media for geological storage of nuclear waste, petroleum, and high-pressure gas. Fundamental deformation processes and flow properties of salt were investigated at the crystal scale (Carter and Hansen, 1983). Constitutive models were also proposed to assess the long-term performance of salt caverns at the field scale (e.g., Bérest et al., 2001; Zhu et al., 2015; Martin et al., 2015). But few numerical studies exist to correlate microscopic phenomena occurring at the grain scale to salt behavior observed at the macroscopic scale.

Microstructure-enriched models allowed better understanding the influence of grain size, orientation, shape, and boundary topology in polycrystalline materials. Finite Element (FE) models are only available for with simple grain geometries, with squared or cubic meshes (e.g., Beaudoin et al., 1995). Such methods ignore the influence of real microstructure on the macroscopic behavior of the polycrystal.

To study the deformation and strength of polycrystals at multiple scales with Finite Element Methods (FEM), discontinuities were modeled with Cohesive Zone Models (Espinosa and Zavattieri, 2003) and extended Finite Element Methods (XFEM) (Sukumar et al., 2003). Metals were extensively studied with microstructure-based FEM, but not salt. Indeed, accounting for the time-dependent viscous damage in salt polycrystals subjected to long-term creep loading remains a major challenge in FEM. Only a few studies are based on a realistic representation of microstructure and investigate inter- and intra-granular damage (Musienko and Cailletaud, 2009).

In this paper, we present a FE model in which microscopic observations of salt thin sections serve as a basis to design the mesh. The model, designed with POROFIS, contains surface elements to represent the grains of consolidated salt, joint elements to model the inter-granular contacts, and voids. We compare three strategies to predict microscopic damage in the salt polycrystal: (1) inter-granular damage represented by damage propagation in joint elements; (2) intra-granular damage represented by stiffness degradation in grain surface elements; (3) damage in both surface and joint elements. The structure of this paper is organized as follows: Section 2 describes the deformation mechanisms in a single crystal of salt; Section 3 presents

the joint-enriched FEM model; Section 4 summarizes the results of simulations obtained with the three numerical models for the prediction of viscous damage in salt subjected to the creep loading.

## 2. DEFORMATION MECHANISMS IN A SINGLE CRYSTAL

The total strain rate of a single crystal of salt ('salt grain') is the sum of the elastic strain rate and the viscoplastic strain rate:

$$\dot{\varepsilon} = \dot{\varepsilon}^{e} + \dot{\varepsilon}^{vp} \tag{1}$$

In most polycrystalline materials, slip is the primary factor of deformation. The viscoplastic strain rate of the grain is the sum of the shear strain rates induced by all possible slip systems:

$$\dot{\varepsilon}_{ij}^{vp} = \sum \dot{\gamma}^{l} a_{ij}^{l} \tag{2}$$

$$a_{ij}^{l} = \frac{1}{2}(m_i^l n_j^l + n_i^l m_j^l) \tag{3}$$

in which $\dot{\gamma}^{l}$ is the viscoplastic strain rate for the $l^{th}$ slip mechanism in a grain. $\boldsymbol{m^l}$ and $\boldsymbol{n^l}$ are the orthonormal unit vectors that define the slip direction and the normal to the slip system, respectively.

Salt crystals have a typical face-centered cubic (FCC) structure. Slip during grain shear deformation occur along six preferential planes, two of which are independent slip systems. Following many experimental observations, irreversible shear deformation is assumed to obey a power law (e.g., Kalidindi et al., 1992):

$$\dot{\gamma}^{l} = \gamma_0 h^{l} \left|\frac{\tau^{l}}{\tau_0}\right|^{n} \tag{4}$$

in which $n$ refers to the sensitivity of the slip rate, $\gamma_0$ is a reference strain rate, $\tau_0$ is a reference shear stress arbitrarily set equal to 1 MPa, and $h^l$ depends on the sign of $\tau^l$: $h^l = 1\ (\tau^l > 0);\ h^l = -1\ (\tau^l \leq 0)$.

The orientation of each grain can be described by Euler angles $(\phi, \theta, \psi)$. In two-dimensions, angles $(\phi, \psi)$ are zero. Therefore, representative grain orientations are obtained by rotation about the normal to the plane of study (Fig. 1).

In the two-dimensional space, shear deformation is governed by two of the six slip systems (Fig. 2), which only differ by a rotation angle of 90 degrees. $\boldsymbol{N}$ and $\boldsymbol{M}$ are the normal and the glide vectors in the local coordinate system of the grain.

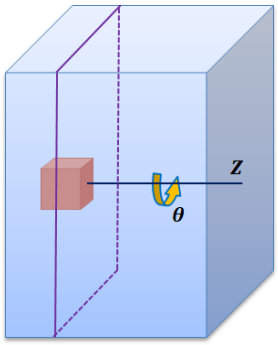


Fig. 1. 2D salt polycrystal. Grain orientation depends on one degree of freedom: the angle of rotation $\theta$ about the $z$ axis.


Fig. 2. The two slip systems governing grain-scale shear deformation in 2D.

In the global coordinate system, for a given angle $\theta$, the two slip systems $(\boldsymbol{n^1}, \boldsymbol{m^1})$ and $(\boldsymbol{n^2}, \boldsymbol{m^2})$ are:

$$\boldsymbol{n^1} = \begin{pmatrix} cos(\theta + \frac{\pi}{4}) \\ sin(\theta + \frac{\pi}{4}) \end{pmatrix},\quad \boldsymbol{m^1} = \begin{pmatrix} cos(\theta + \frac{3\pi}{4}) \\ sin(\theta + \frac{3\pi}{4}) \end{pmatrix}$$
$$\boldsymbol{n^2} = \begin{pmatrix} cos(\theta + \frac{3\pi}{4}) \\ sin(\theta + \frac{3\pi}{4}) \end{pmatrix},\quad \boldsymbol{m^2} = \begin{pmatrix} cos(\theta + \frac{\pi}{4}) \\ sin(\theta + \frac{\pi}{4}) \end{pmatrix} \tag{5}$$

## 3. JOINT-ENRICHED FINITE ELEMENT MODEL

We used POROFIS (Pouya, 2015) to model a sample of thermally consolidated salt that was fabricated and observed in the Department of Geology and Geophysics at Texas A&M University. Salt grains and grain boundaries were represented by surface elements and joint elements, respectively. We hypothesize that creep deformation is due to crack propagation, and we simulate creep tests with several damage models in order to understand whether cracks primarily propagate inside the grains or at inter-granular interfaces (Table 1).

Table 1. Three finite element models based on different damage mechanisms.

| Model Number | Inter-granular | Intra-granular |
|---|---|---|
| Model 1 | Damageable joint elements | Visco-elastic surface elements |
| Model 2 | Elastic joint elements | Visco-damageable surface elements |
| Model 3 | Damageable joint elements | Visco-damageable surface elements |

### *3.1. Inter-granular damage*

For the damageable joint elements, we adopted the strength model developed by Pouya and Yazdi (2015), in which strength evolves with damage as:

$$F(\sigma, D) = \tau^2 - \sigma_n^2 tan^2\eta + 2g(D)\sigma_c\sigma_n - g^2(D)C^2 \quad (6)$$

$$g(D) = (1-D)(1-\beta ln(1-D)) \quad (7)$$

in which $C$ is the cohesion and $\eta$ is the friction angle. $D$ is the damage variable in the rock joint. $g(D)$ takes the value 1 for the initial non-damage state ($D = 0$) and 0 for the ultimate failure state ($D = 1$). The shape parameter $\sigma_c$ of the yield surface relates to $C$, $\eta$, and the tensile strength $\sigma_R$ of the intact rock joint, as follows:

$$\sigma_c = \frac{C^2 + \sigma_R^2 tan^2\eta}{2\sigma_R} \quad (8)$$

In Fig. 3, the outer hyperbolic surface corresponds to the initial intact state $(g = 1, D = 1)$. The yield surface moves inwards when damage increases. For the limiting state of a completely damaged joint, the resulting fracture has zero cohesion and the friction angle satisfies:

$$F(\tau, \sigma_n) = \tau^2 - \sigma_n^2 tan^2\eta \quad (9)$$

As indicated in Fig. 3, the tensile strength and the cohesion parameter satisfy the following inequality:

$$C > \sigma_R \tan\eta \quad (10)$$

Similar to the choice of damage in the interfaces of cementitious materials (Jefferson, 1998), damage is assumed to evolve according to an exponentional function of the relative displacement:

$$D = 1 - e^{-(u-u_0)/\beta u_0} \quad (11)$$

in which the constant parameter $\beta$ characterizes the material ductility (the smaller $\beta$, the more brittle the material behavior).

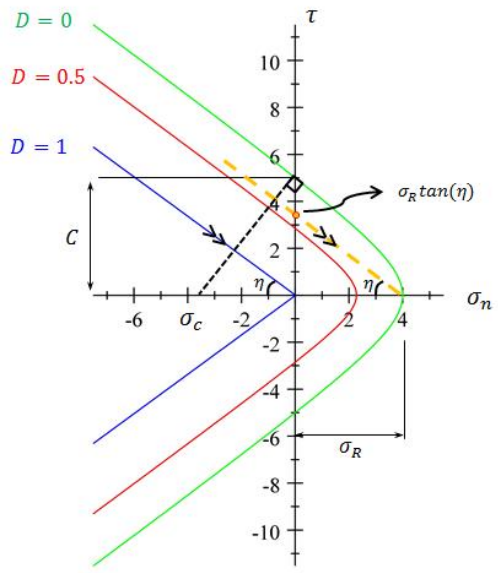


Fig. 3. Damage-plasticity criterion used in the joint elements: from the intact state (*D=0*) to failure (*D=1*).

### *3.2. Intra-granular damage*

Damage inside the grains is induced by incompatibilities of the viscous strain of neighboring grains and the resulting local stress concentrations. After damage initiates, the grain stiffness gradually decreases and eventually drops to a negligible value. To capture this phenomenon, we used a model of stiffness degradation in the surface elements. A grain element is completely broken and can be treated as a void when its damage variable $D_g$ increases to 1.

We assume that damage remains equal to zero up to a critical visco-plastic deformation, and increases exponentially with deformation as:

$$D_g = 1 - e^{-(\varepsilon^{vp} - \varepsilon_0^{vp})/\chi\varepsilon_0^{vp}} \quad (12)$$

in which the rate of damage is:

$$\dot{D}_g = \frac{1}{\chi\varepsilon_0^{vp}} \|\dot{\boldsymbol{\varepsilon}}^{\boldsymbol{vp}}\| e^{-(\varepsilon^{vp} - \varepsilon_0^{vp})/\chi\varepsilon_0^{vp}} \quad (13)$$

This model couples damage and visco-plasticity in the grain. Different rates of visco-plastic deformation are used for secondary and tertiary creep. The threshold between these two creep regimes is calibrated by means of micro-macro model (Pouya et al., 2016). We determined the critical visco-plastic deformation $\varepsilon_c^{vp}$ for creep tests under various axial stresses and established a relationship between $\varepsilon_c^{vp}$ and creep load $\sigma_c$ at a material point. The deformation threshold obeys a bilinear form (Zhu et al., 2015):

$$\varepsilon_c^{vp} = 5 \times 10^{-5}\sigma_c - 2 \times 10^{-5} \quad (2 \le \sigma_c \le 4.78) \quad (14)$$

$$\varepsilon_c^{vp} = 4 \times 10^{-6}\sigma_c + 2 \times 10^{-4} \quad (\sigma_c > 4.78) \quad (15)$$

### 3.3. *Image analysis and meshing*

Dry granular salt specimens were consolidated under different temperature and loading conditions. The average grain size was 1.7~2.0 mm. After consolidation, samples were first saturated with blue epoxy resin to enhance the grain and void interfaces, and then polished and cleaned with isopropyl alcohol. The typical thickness of a thin section was about 200 micrometers.

We selected a thin section micrograph that presented a relative homogeneity (Fig. 4). This specimen was consolidated at 200°C under 52 MPa for about 10 minutes. The resulting porosity after consolidation was 6%. Intra-granular cracks can be observed in some grains as a result of the consolidation, which highlights the importance of accounting for intra-granular damage in the grain FEs.

In order to minimize boundary effects, we constructed a 2D FEM polycrystal model of the central region of the micrograph (bounded by a square in Fig. 4). We used the software *Plot Digitizer* to extract grain and void boundaries from the microstructure image and export them into GiD FEM pre- and post-processor (GiD, 2002) for meshing.

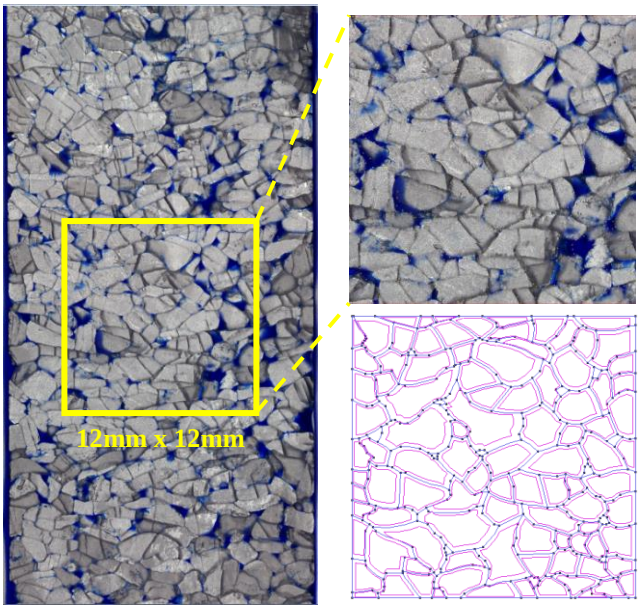


Fig. 4. Thin section image of consolidated granular salt saturated with blue epoxy. Left: Grey regions represent granular salt particles while blue areas filled with epoxy indicates inter-granular pores. Right: The FEM mesh was generated with *Plot Digitizer* and *GiD*.

Since the section selected was relatively homogeneous, we assumed that grain orientations in the mesh followed a uniform distribution. For simplicity, we used 12 grain orientations, i.e., 12 cosine values of $\theta$ uniformly distributed in the interval $[cos(\theta = 0) = 0, cos(\theta = \frac{\pi}{2}) = 1]$. We assigned a grain orientation of the surface elements in such a way that the distribution of grain orientations be relatively isotropic and homogeneous (Fig. 5). We also used joint elements along grain boundaries.

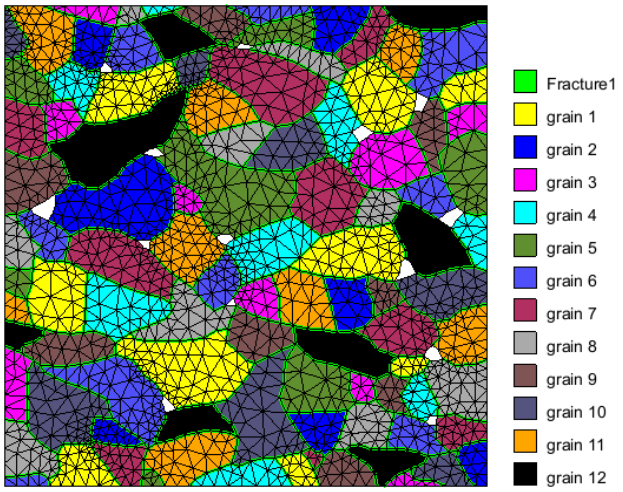


Fig. 5. Joint-enriched finite element model (12mm × 12mm). In the legend, grain numbers refer to grain orientations. Fracture 1 is the inter-granular joint element. Empty spaces (white color) represent the inter-granular voids.

### 3.4. *Model calibration*

We used published experimental data to calibrate (a) the elastic properties, viscous parameters, and damage parameters of the grain surface elements; (b) the stiffness and strength parameters of the joint elements. The procedure is the following:

1. The stiffness of the joint elements was determined by comparing the Young's modulus of the region modeled to that of specimens tested experimentally.
2. The viscous parameters of the grain surface elements were fitted so as to match the steady state strain rate measured in experiments.
3. The damage parameters of grain surface elements and the strength of joint elements were calibrated by determining the time of tertiary creep initiation and matching the tertiary creep curve obtained experimentally.

The calibration process depends on both steady state and tertiary state of the creep test results (Zhu et al., 2016). Table 2 summarizes the material parameters calibrated for the joint-enriched finite element model designed with POROFIS.

Because joints are essentially contacts among grains and their physical properties are experimentally challenging to measure, the calibration process still requires further improvement in order to apply this model for more practical problems.

Table 2. Material parameters calibrated for the POROFIS model.

| Grain | | | |
|---|---|---|---|
| $E$ (GPa) | $\nu$ (-) | $\gamma_0$ (day$^{-1}$) | $n_1$ (-) |
| $4.3 \times 10^4$ | 0.3 | $2.0 \times 10^{-5}$ | 4.0 |
| $B$ (day$^{-1}$) | $n_2$ (-) | $\chi$ (-) | |
| $1.0 \times 10^{-8}$ | 6.9 | 115 | |
| Inter-granular joint | | | |
| $k_t$ (MPa/mm) | $k_n$ (MPa/mm) | $e$ (mm) | $\sigma_R$(MPa) |
| $1.0 \times 10^4$ | $1.0 \times 10^5$ | 0.1 | 6.13 |
| $C$ (MPa) | $\eta$ (degrees) | $\beta$ (-) | $k_{tn}$ (MPa/mm) |
| 6.13 | 30 | 1.0 | 0 |

Notations:

| | |
|---|---|
| $E$ | Young's modulus |
| $\nu$ | Poisson's ratio |
| $\gamma_0, n_1$ | Viscous parameters of grains |
| $B, n_2, \chi$ | Damage parameters of grains |
| $k_t, k_n, k_{tn}$ | Joint stiffness |
| $e$ | Joint thickness |
| $\sigma_R$ | Tensile strength of intact joints |
| $C$ | Cohesion of intact joints |
| $\eta$ | Friction angle of intact joints |
| $\beta$ | Material ductility |

## 4. NUMERICAL STUDY OF VISCOUS DAMAGE IN SALT

In the following simulations, the polycrystal is subjected to a rapid monotonic loading followed by a uniaxial creep load of 5 MPa applied for 0.3 days – which is a typical operation pressure at a geological site for Compressed Air Energy Storage. The creep loading is applied uniformly at both the upper and lower boundaries of the model presented in Section 3 (Fig. 5). Horizontal displacements are fixed ($U_x = 0$) for the central nodes of the upper and lower boundaries. Vertical displacement is fixed ($U_y = 0$) for the central node along the right boundary.

We compare the results obtained with the three models presented in Table 1 at two key times: (1) at the end of the monotonic loading phase (t = 0.005d, point A); (2) during the creep process (t = 0.24d, point B).

At point A, the stress and displacement fields are the same with the three models (Fig. 7). This is because both grains and joints remain intact at this initial stage ($D = D_g = 0$). Under the influence of uniaxial stress imposed at the top and bottom of the domain, grains expand laterally, which induces tensile stress at grain boundaries, mostly in the direction that is parallel to the loading axis (Fig. 7a). Grains adjacent to voids undergo less deformation constraints. Compressive stress concentrations appear at the grain boundaries where grain shapes are highly irregular or where several angular grains are in contact. Because of the distribution of the crystal orientations, the displacement field within the grains is antisymmetric about the central axis of the polycrystal (Fig. 7b).

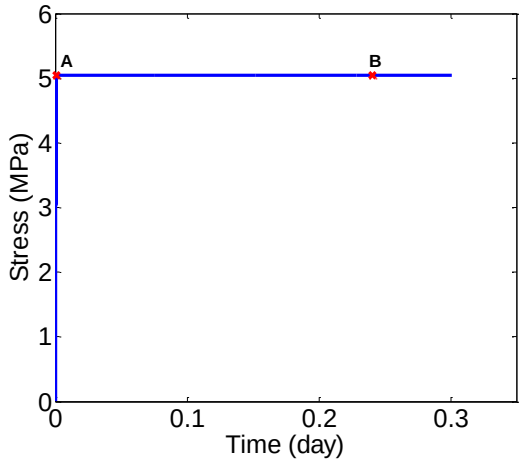


Fig. 6. Stress time history imposed in the creep simulations. Point A marks the transition between the monotonic increasing stress loading and creep loading phases (t = 0.005d). Point B is during the creep process (t = 0.24d).

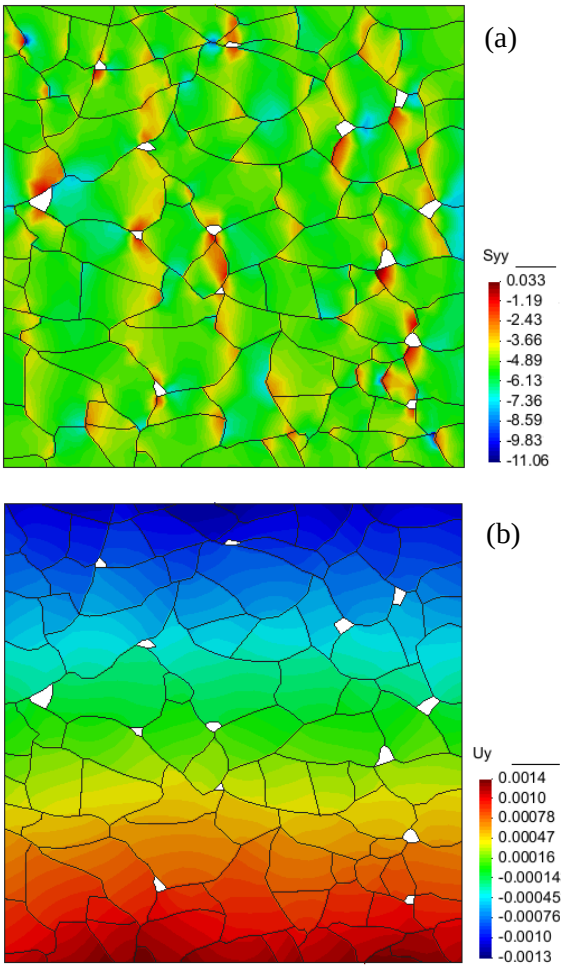


Fig. 7. Results at the end of monotonic loading phase at t = 0.005d – Point A (same for the three models): (a) stress (MPa); (b) displacement (mm). Note: compression is negative with *POROFIS*.

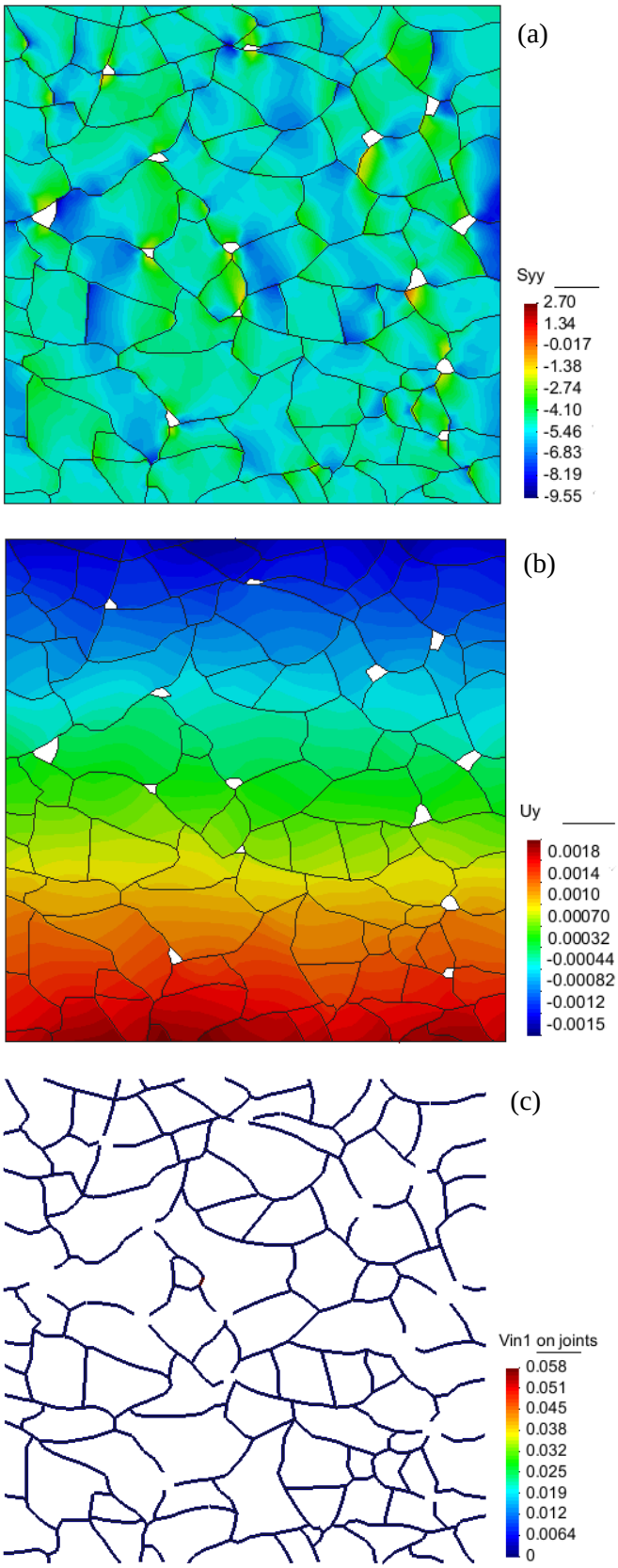


Fig. 8. Results of model 1 (damage in joints only) during the creep process at t = 0.24d - Point B: (a) stress (MPa); (b) displacement (mm); (c) damage in joint elements.

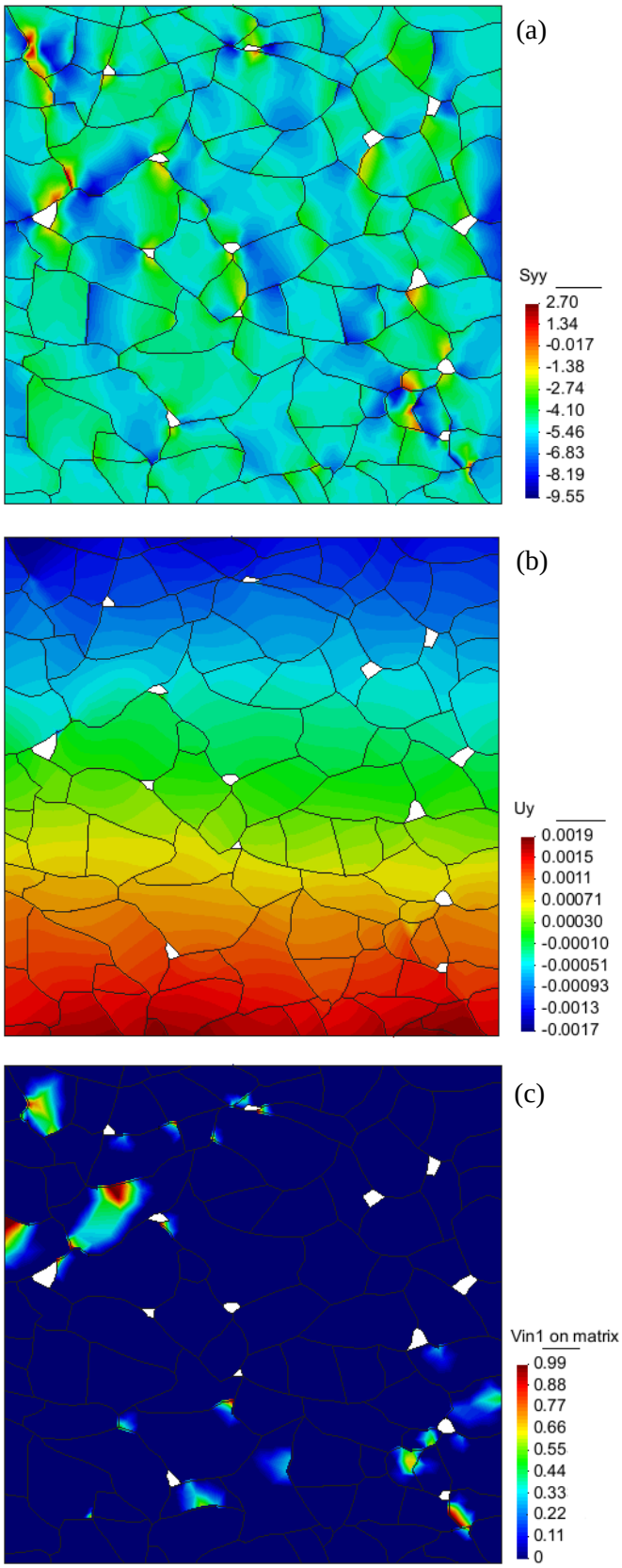


Fig. 9. Results of model 2 (damage in grains only) during the creep process at t = 0.24d - Point B: (a) stress (MPa); (b) displacement (mm); (c) damage in grain elements.

When the creep process starts, viscoplastic deformation in grains evolves. We continue to observe strong concentrations of vertical stresses at the contact of

angular grains. This results in inter-granular slip and subsequent damage in joints and grains. Using the same stress scale in the legends of Fig. 8a, 9a, 10a, it can be seen that stress distributions and concentrations are similar in the three models. The highest tensile stress concentrations appear in model 2 at the locations where voids exist or several angular grains are in contact. This is due to the fact that unlike in models 1 and 3, energy cannot be dissipated by crack propagation in the joints. Energy accumulates until sudden dissipation occurs through grain breakage, leading to a brittle response.

The contours of displacement fields are almost the same in the three models (Fig. 8b, 9b, 10b). Models 2 and 3 experience relatively higher deformation than model 1 since broken grains behave like voids, which allows neighboring grains to rearrange significantly.

The three models differ for the prediction of damage accumulation at point B (t = 0.24d), under the same loading magnitude and for the same loading period (Fig. 8c, 9c, 10c and 10d). In the absence of energy dissipation in the joints, model 2 is exposed to a considerable amount of damage in the grains. By contrast, as shown in Fig. 10d, grains in model 3 undergo less damage since inter-granular joint breakage contributes to energy dissipation. In model 3, damage accumulates faster in grains than in joints and most joints remains undamaged at point B.

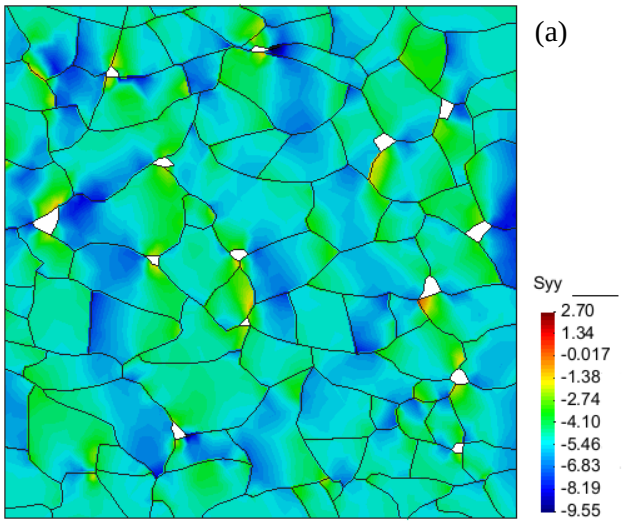


Fig. 10. Results of model 3 (damage in joints and grains) during the creep process at t = 0.24d - Point B: (a) stress (MPa); (b) displacement (mm); (c) inter-granular damage in joint elements; (d) intra-granular damage in grain elements.

In order to obtain the creep curve of the polycrystal modeled with POROFIS, we calculated the average values of strains over the entire set of integration points. The plots of strain-time history for the three models during the creep phase are shown in Fig. 11. In model 1,

the polycrystal remains in the steady state creep regime whereas tertiary creep is reached in models 2 and 3. With intra-granular damage mechanism only, model 2 presents the most brittle failure and reaches tertiary state at t = 0.24d, which shows a good agreement with the rapid damage accumulation in grain elements shown in Fig. 9c. Although the creep curve obtained from model 3 matches the general trend of the curve obtained with model 2, the transition between steady state and tertiary state is much smoother. This indicates the importance of accounting for inter-granular slip-induced damage in joints for salt polycrystals. However, the impact of intra-granular damage observed in the experiments cannot be ignored (Fig. 4). As shown in Fig. 11, results obtained with model 1 reveal a completely different behavior: the polycrystal is very ductile and remains almost undamaged (Fig. 8c). Future work will concentrate on the validation of these results, in particular the prediction of deformation at the macroscopic scale and fracture patterns at the microscopic scale.

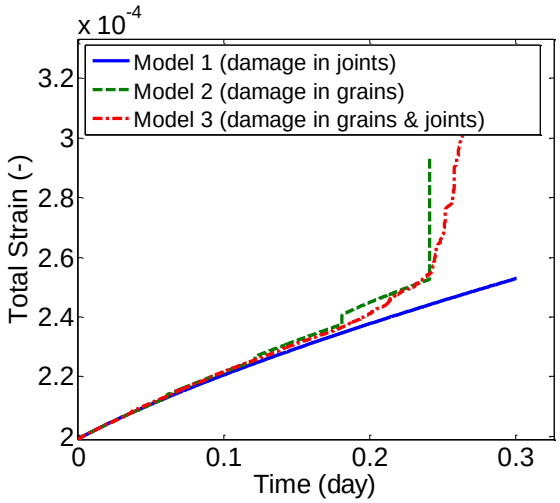


Fig. 11. Creep curves obtained with the three models. Note that the strains from the initial monotonic loading phase are the same for the three models and not shown in this figure.

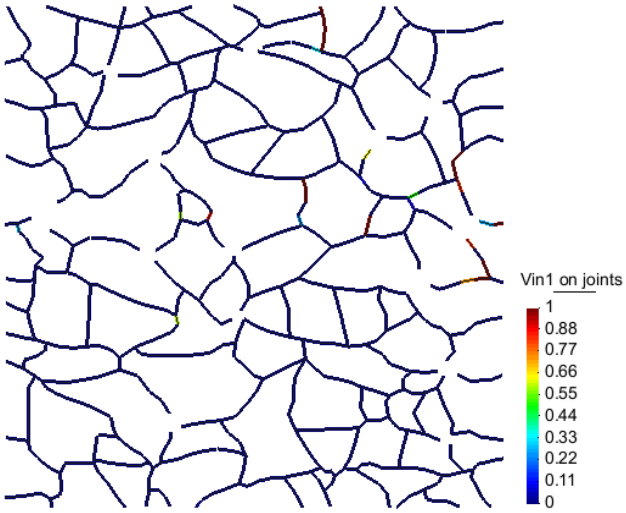


Fig. 12. Damage in joints of model 1 at ultimate failure (t = 6.68d).

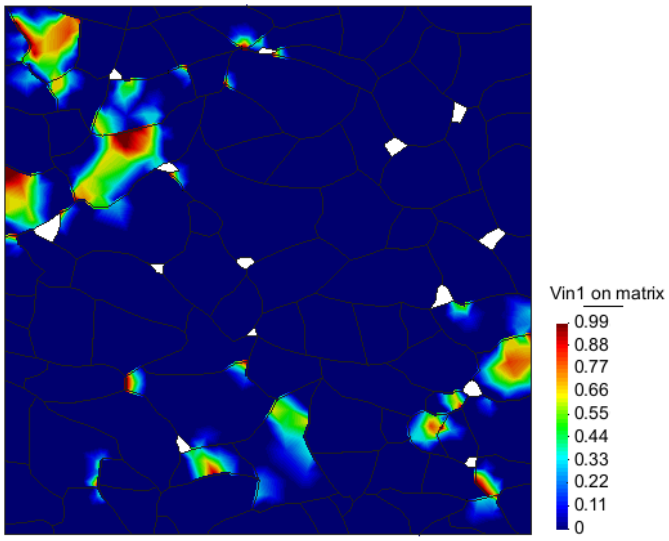


Fig. 13. Damage in grains of model 2 at ultimate failure (t = 0.25d).

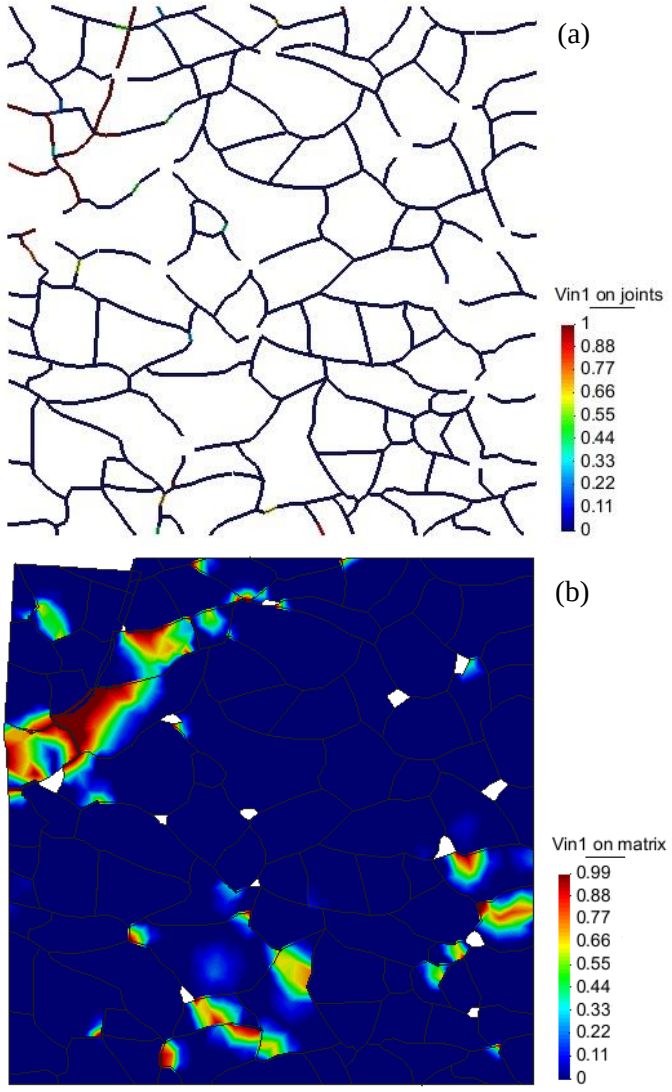


Fig. 14. Results of model 3 at ultimate failure (t = 0.276d): (a) damage in joints; (b) grain damage in the deformed shape.

The rapid deformation observed during tertiary creep is the result of accelerated damage accumulation at the microscopic level. We continued the simulations until failure with the three models. We find that model 1 requires the longest time to reach failure (6.68 days, against 0.276 days with model 3 and 0.25 days with model 2). With model 1, most damaged joints are parallel to the creep loading direction. At failure, some damaged joints have coalesced with the pre-existing voids (Fig. 12). The ultimate damage distribution in model 2 exhibits only a few damage zones. The highest damage values are observed in the upper left region of the polycrystal, maybe because of the local heterogeneities (Fig. 13). Similar damage distributions in the grains are obtained with model 3 (Fig. 14b). In model 3, high stress concentrations not only lead to grain stiffness weakening, but also inter-granular damage (Fig. 14a). As a result of the coalescence of damaged joints and voids, the upper left portion tends to slip downward, along joint interfaces, which causes ultimate failure in model 3 (Fig. 14b).

## 5. CONCLUSIONS

In this study, we used a joint-enriched Finite Element Method to model intra- and inter- granular crack propagation in salt subjected to creep loading. Intra-granular damage is represented by the gradual degradation of stiffness of the grain surface elements. Inter-granular damage propagation is captured by damageable joint elements. Dry granular salt specimens were consolidated under controlled conditions of stress and temperature in order to obtain synthetic salt rock. Thin sections were observed with a microscope. Grain contours obtained from microscope image analysis define the geometry of the joint elements used in the mesh. Grain surface elements have different crystal orientations, which are assigned a uniform distribution.

Constitutive parameters of the surface and joint element models were calibrated against published experimental data, so as to match the steady state and tertiary state strain rates and the initiation of tertiary state during creep processes.

We simulated a creep test with three FEM models that account for inter-granular damage only, intra-granular damage only, and both inter- and intra-granular damage, respectively. At the contact between several angular grains or at the contact between grains and a void, stress concentrations result in inter-granular slip. Through damage evolution in the grains or in inter-granular interfaces, the proposed joint-enriched FEM model captures the multiscale mechanical behavior of the polycrystal under creep loading, in particular: crack initiation, propagation, and coalescence at the microscopic scale, and steady state and tertiary state creep deformation at macroscopic scale. Models with damageable joints exhibit a more ductile response with a smoother transition between steady state and tertiary creep. If grains are represented by elastic surface elements, intra-granular damage that has been observed experimentally cannot be captured and, provided that damage can occur on the grain boundary joint elements, macroscopically the simulated behavior is very ductile. In all models, at the end of the creep test, viscous shear deformation in the grains induces important geometric incompatibilities, which results in higher local stresses, faster damage accumulation, and ultimately the failure of the polycrystal.

Our future work will focus on the Finite Element modeling of multi-sale damage processes during thermal consolidation of dry salt, before creep loading. Dry consolidation has been poorly investigated so far, due to numerous experimental challenges, which include moisture control during and after consolidation for microscopic imaging, time-consuming experimental process and crack localization that can abruptly break the sample. Numerically, challenges are mostly calibration, convergence, and stability. Image analysis is the key to explain the formation of fracture patterns and to correlate microstructure evolution to macroscopic deformation regimes. Rigorous numerical studies will provide recommendations on the best strategies to capture grain damage, plasticity, rearrangement, slip, indentation, and inter-granular cracks.

## ACKNOWLEDGEMENTS

Financial support for this research was provided by the National Science Foundation (Grant No. CMMI-1362004/1361996).

## REFERENCES

1. Beaudoin, A., P. Dawson, K. Mathur, and U. Kocks. 1995. A hybrid finite element formulation for polycrystal plasticity with consideration of macrostructural and microstructural linking. *International Journal of Plasticity*. 11 (5): 501-521.

2. Bérest, P., J. Bergues, B. Brouard, J. Durup, and B. Guerber. A salt cavern abandonment test. *International Journal of Rock Mechanics and Mining Sciences*. 38 (3): 357-368.

3. Carter, N.L. and F. D. Hansen. 1983. Creep of rock salt. *Tectonophysics*. 92 (4): 275-333.

4. Espinosa, H.D. and P. D. Zavattieri. 2003. A grain level model for the study of failure initiation and evolution in polycrystalline brittle materials. Part I: Theory and numerical implementation. *Mechanics of Materials*. 35: 333-364.

5. GiD. 2002. The personal pre- and post-processor. International Center for Numerical Methods in Engineering (CIMNE). www.gidhome.com.

6. Jefferson, A. 1998. Plastic-damage model for interfaces in cementitious materials. *Journal of Engineering Mechanics*. 124 (7): 775-782.

7. Kalidindi, S.R., C.A. Bronkhorst, and L. Anand. 1992. Crystallographic texture evolution in bulk deformation processing of FCC metals. *Journal of the Mechanics and Physics of Solids*. 40 (3): 537-569.

8. Martin, L.B., R. Wolter, J. Rutqvist, K.-H. Lux, and J. T. Birkholzer. 2015. Comparison of two simulators to investigate thermal-hydraulic-mechanical processes related to nuclear waste isolation in saliferous formations. *Computers and Geotechnics*. 66: 219-229.

9. Musienko, A. and G. Cailletaud. 2009. Simulation of inter- and transgranular crack propagation in polycrystalline aggregates due to stress corrosion cracking. Acta Materialia. 57: 3840-3855.

10. Pouya, A. 2015. A finite element method for modeling coupled flow and deformation in porous fractured media. *International Journal for Numerical and Analytical Methods in Geomechanics*. 39 (16): 1836-1852.

11. Pouya, A. and P. B. Yazdi. 2015. A damage-plasticity model for cohesive fractures. *International Journal of Rock Mechanics and Mining Sciences*. 73: 194-202.

12. Pouya, A., C. Zhu, and C. Arson. 2015. Micro-macro approach of salt viscous fatigue under cyclic loading. *Mechanics of Materials*. 93: 13-31.

13. Sukumar, N., D. J. Srolovitz, T. J. Baker, and J.-H. Prevost. 2003. Brittle fracture in polycrystalline microstructures with the extended finite element method. *International Journal for Numerical Methods in Engineering*. 56: 2015-2037.

14. Zhu, C., A. Pouya, and C. Arson. 2015. Micro-macro analysis and phenomenological modelling of salt viscous damage and application to salt caverns. *Rock Mechanics and Rock Engineering*. 48 (6): 2567-2580.

15. Zhu, C., A. Pouya, and C. Arson. 2016. Comparison between inclusion-matrix modeling and Finite Element Method for viscous damage and fatigue in salt rock. *Mechanics of Materials*. (under review).